The Astrophysical Journal Letters, 917:L31 (7pp), 2021 August 20 https://doi.org/10.3847/2041-8213/ac1859

Beamed Emission from a Neutron-star ULX in a GRRMHD Simulation

David Abarca[1], Kyle Parfrey[2], and Włodek Kluźniak[1]
[1] Nicolaus Copernicus Astronomical Center of the Polish Academy of Sciences, Bartycka 18, 00-716 Warsaw, Poland; dabarca@camk.edu.pl
[2] School of Mathematics, Trinity College Dublin, Dublin 2, Ireland
Received 2021 June 25; revised 2021 July 22; accepted 2021 July 28; published 2021 August 20

Abstract

We perform a global 2.5D general-relativistic radiation magnetohydrodynamic simulation of supercritical accretion onto a neutron star with a 2×10^{10} G dipolar magnetic field, as a model of a neutron-star-powered ultraluminous X-ray source (ULX). We compute a lower limit on the total luminosity of $\sim 2.5\, L_{\rm Edd}$, and find the radiation to be highly beamed by the accretion disk outflows. The apparent isotropic luminosity, which is a function of the viewing angle, reaches a maximum above $100\, L_{\rm Edd}$, consistent with the luminosities observed in ULXs.

Unified Astronomy Thesaurus concepts: Ultraluminous x-ray sources (2164); Magnetohydrodynamical simulations (1966); Neutron stars (1108)

1. Introduction

Ultraluminous X-ray sources (ULXs) are extragalactic, non-active-galactic-nucleus X-ray sources with luminosities exceeding 10^{39} erg s^{-1} (Kaaret et al. 2017). Observations, in a handful of ULXs, of coherent pulsations of $\sim$1 s periodicities (Trudolyubov 2008; Bachetti et al. 2014; Motch et al. 2014; Fürst et al. 2016; Israel et al. 2017a, 2017b; Townsend et al. 2017; Tsygankov et al. 2017; Brightman et al. 2018; Carpano et al. 2018; Doroshenko et al. 2018; Fürst et al. 2018; Heida et al. 2019; Chandra et al. 2020) have shown that at least some of these sources are powered by slowly rotating neutron stars accreting above their critical limits, $\dot{M}_{\rm Edd} = \eta L_{\rm Edd}/c^2$, where $\eta \sim 0.2$ is the binding energy per unit mass at the surface of the neutron star (Syunyaev & Shakura 1986) and $L_{\rm Edd} = 4\pi GMm_p c/\sigma_T$ is the Eddington luminosity of an object with mass M.

For low accretion rates η is also the expected radiative efficiency, and the luminosity is proportional to the mass accretion rate, $L/L_{\rm Edd} = \dot{M}/\dot{M}_{\rm Edd}$. However, due to their extremely large optical depths, accretion disks with $\dot{M} \gtrsim \dot{M}_{\rm Edd}$ can no longer cool efficiently. The accretion flow traps photons and the advection of radiation becomes the primary mode of energy transport in the disk (Begelman 1978; Abramowicz et al. 1988; Sądowski & Narayan 2016; Czerny 2019). The large concentration of photons launches a radiation-pressure-driven outflow, which originates at the radius where the radiation flux through the surface of the disk becomes super-Eddington (Shakura & Sunyaev 1973). The outflow extends from this radius (referred to as the spherization radius) down to the inner edge of the accretion disk. Because of advection, the value of the spherization radius will differ somewhat from its classic thin-disk value (Shakura & Sunyaev 1973). In fact, a substantial fraction of the photons in the radiation-pressure-dominated inner disk will be advected to the vicinity of the stellar surface and released there. How it escapes to infinity is the major focus of this Letter.

King et al. (2001) suggested long before the first pulsating ULXs were observed that the outflows from a super-Eddington disk could collimate the emission released near the compact object, in a manner similar to the collimation predicted by the thick disk model of the Warsaw group (Abramowicz et al. 1978; Paczyński & Wiita 1980). The system would then appear to be very bright when viewed face-on, and the inferred isotropic luminosity $L_{\rm iso} = F/(4\pi d^2)$, where F is the radiation flux measured by the observer and d is the distance to the source, would be much larger than the true luminosity, L, i.e., the total emitted radiation power.

An additional interesting feature of pulsating ULXs is their unusually high spin-up rates. Kluźniak & Lasota (2015) inferred a dipole field of $\sim 10^9$ G from the spin-up rate of M82 X-2. As more pulsating ULXs were found, all with high spin-ups, a model was formed that incorporated the period, spin-up, and luminosity to predict the magnetic field strength and intensity of the beaming (King et al. 2017; King & Lasota 2019, 2020, hereafter referred to as the KLK model). Besides very small values of the beaming factor $b = L/L_{\rm iso}$—implying a high degree of beaming—the model also predicts dipole magnetic fields in the range of 10^9–10^{13} G, with most values falling between 10^{10} and 10^{11} G.

In order to model a neutron star accreting at super-Eddington accretion rates, it is necessary to run general-relativistic radiative magnetohydrodynamic (GRRMHD) simulations. As of writing this Letter, there is only one such global simulation (Takahashi & Ohsuga 2017) that includes a stellar magnetic field, and two that do not (Abarca et al. 2018; Takahashi et al. 2018).

The simulation discussed in Takahashi & Ohsuga (2017), while an important result, has some shortcomings. It is unclear how the highly magnetized regions are treated, or what effects the numerical density floor or background atmosphere have on the emerging radiation. The simulation is run for a rather short duration, not allowing adequate time for the outflows to reach a steady state. To overcome these issues, all of which could potentially contaminate measurements of the luminosity and flux distribution, we introduce a scheme that captures the highly magnetized regions of the simulation more realistically. Such a scheme was introduced by Parfrey & Tchekhovskoy (2017) and we have implemented it in the GRRMHD code `Koral`. We ensure the numerical floors do not affect the emerging radiation and run the simulation for a much longer duration.

We wish to investigate the degree to which the radiation produced by an accreting magnetized neutron star is beamed. Small values of b and lower neutron-star magnetic fields would support the KLK model, while values of b near unity would indicate that some other configuration must be responsible for

such high observed luminosities. Even if we do find the radiation to be highly beamed, a direct comparison to the KLK model would not be very informative considering the requirement that the magnetospheric and spherization radii be quite close to each other.

A further caveat to consider is that we have aligned the magnetic dipole axis with the disk axis, so even if we included rotation, we would not expect to produce pulsations. However, the population of non-pulsed ULXs is much larger than the population of pulsed ULXs, and there is no reason to believe that some of these also may not be powered by neutron stars.

At the accretion rates we are considering, it has been predicted that the flow to the magnetosphere forms an optically thick "accretion curtain" shielding the stellar surface outside the polar regions (Mushtukov et al. 2017). For a rotating, misaligned dipole, this would produce smooth pulse profiles as the radiation is only able to escape through the thin funnel region along the magnetic poles and this may significantly lower the pulse fraction through multiple scatterings off the funnel wall, making a strong pulsed fraction inconsistent with strong beaming (Mushtukov et al. 2021). A fully 3D simulation with a misaligned dipole would be necessary to adequately address this possible inconsistency.

In Section 2 we describe the numerical methods and the simulation setup. In Section 3 we describe the results of the simulation. In Section 4 we discuss the effects of beaming and the expected observed luminosity of the system, and in Section 5 we summarize the results and our conclusions.

2. Numerical Methods

We use the code `Koral` (Sądowski et al. 2013, 2015), which solves the conservation equations of GRRMHD on a static grid in a fixed metric, $g_{\mu\nu}$. The evolution equations are given by

$$\nabla_\mu(\rho u^\mu) = 0, \tag{1}$$

$$\nabla_\mu T^\mu{}_\nu = G_\nu, \tag{2}$$

$$\nabla_\mu R^\mu{}_\nu = -G_\nu, \tag{3}$$

$$\nabla_\mu F^{*\mu\nu} = 0. \tag{4}$$

The equations correspond to conservation of mass, conservation of total energy-momentum with coupling of matter and radiation provided by the radiation four-force, G_ν, (Mihalas & Mihalas 1984), and the source-free Maxwell's equations. Conservation of mass depends on ρ, the baryon rest-mass density, and u^μ, the gas four-velocity. The stress-energy tensor for a magnetized gas is given by

$$T^\mu{}_\nu = (\rho + p + u_{\rm int} + b^2)u^\mu u_\nu + (p + b^2/2)\delta^\mu_\nu - b^\mu b_\nu, \tag{5}$$

which makes use of $u_{\rm int}$, the gas internal energy, $p = (\gamma - 1)u_{\rm int}$, the gas pressure (where $\gamma = 5/3$ is the adiabatic index), and the magnetic field four-vector, $b^\mu = \frac{1}{2}u_\nu F^{*\mu\nu}$.

Written in terms of the Hodge dual of the Faraday tensor, $F^{*\mu\nu}$, the source-free Maxwell equations correspond to the induction equation (spatial components), and the divergence-free condition of the magnetic field (t component), both of which are evolved using the flux constrained transport algorithm (Tóth 2000).

Equation (3) only evolves the $R^{t\mu}$ components of the radiation stress-energy tensor using G_ν, which includes opacities defined by electron scattering, Comptonization, and bremsstrahlung absorption. The spatial components, R^{ij}, are computed using the M_1 closure scheme (Mihalas & Mihalas 1984; Sądowski et al. 2013), which makes the approximation that there exists a frame with four-velocity $u^\mu_{\rm R}$ in which the radiation can be considered to be isotropic. In that frame, the radiation has energy density $\bar{E}$. We can then write the radiation tensor in the lab frame as

$$R^{\mu\nu} = \frac{4}{3}\bar{E}u^\mu_{\rm R}u^\nu_{\rm R} + \frac{1}{3}g^{\mu\nu}\bar{E}, \tag{6}$$

which can be inverted to give the radiation primitive variables $\bar{E}$ and $u^\mu_{\rm R}$ in terms of $R^{t\mu}$.

Since we study a nonrotating star[3] it is sufficient to use the Schwarzschild metric with a coordinate system that is logarithmic in radius and stretches from $r = 5\,r_g$ to $r = 1000\,r_g$, where $r_g = GM\,c^{-2}$ is the gravitational radius defined by the neutron-star mass M. For the purposes of this calculation we take the radius of the star to be $R = 5r_g$ and we specify[4] its mass at the canonical value 1.4 $M_\odot$. While modern studies with the NICER instrument indicate $R \approx 6.4\,r_g$ at $M \approx 1.3\,M_\odot$ (Riley et al. 2019), the adopted value of M or R does not affect our results qualitatively. In this work the geometry of accretion is controlled by the magnetosphere.[5] Unless otherwise specified, we adopt units where $G = c = 1$. Our simulation is run in 2D axisymmetry with resolution in r and θ corresponding to [512, 510] cells.

We initialize the simulation with an equilibrium torus (Penna et al. 2013) threaded by a single loop of magnetic field that feeds gas to the star at a rate of $\sim 20\dot{M}_{\rm Edd}$. The initial maximum $\beta = (p_{\rm gas} + p_{\rm rad})/p_{\rm mag}$ (the ratio of gas plus radiation to magnetic pressures) in the torus is equal to 10. We initialize a stellar dipole field with a maximum field strength on the stellar surface of 2×10^{10} G using the potential given in Wasserman & Shapiro (1983).

Outside the torus, the gas is initialized to a low-density background. This creates a large contrast in the magnetic and rest-mass energy densities. The ratio of these two quantities, the magnetization, $\sigma = b^2/(2\rho)$, provides an indication of where the numerical scheme should start to break down, with $\sigma \gg 1$ regions being especially prone to error/instabilities. Our simulation is initialized with a peak magnetization of $\sigma = 10^4$, and in order to evolve the system we implement the method described in Parfrey & Tchekhovskoy (2017). The basic idea of the scheme is to divide the gas into contributions from the real general-relativistic magnetohydrodynamic (GRRMHD) flow and from the numerical floor that keeps σ from becoming too large. When gas is dominated by the numerical floor, the density and internal energy are adjusted to their background levels and the velocity parallel to the magnetic field, as measured by the stationary observer, is reduced. We provide some additional adjustments that improve the scheme's robustness in the presence of radiation. We reduce the scattering and absorption opacities of the gas dominated by the numerical floor, and we balance energy gain/loss from round-off errors in the magnetic field by respectively subtracting/adding

[3] The observed ULX periods of several seconds make the spin of the neutron star negligible in our simulations, which typically run for about $\sim 10^5\,GM\,c^{-3}$, i.e., $\sim$0.7 s of physical time.

[4] The results of radiative simulations do not scale with the stellar mass, which therefore must be specified.

[5] In general R/r_g varies with the stellar mass, and it is only for weakly magnetized stars (with a dipole moment about two orders of magnitude below what we assume here) that the character of flow depends on whether R is larger or smaller than the radius of the marginally stable orbit (Kluzniak & Wagoner 1985).

radiation energy during the conserved-to-primitive variable inversion.

We also introduce a new boundary condition that attempts to mimic the hard surface of the neutron-star crust. We treat the gas as in Parfrey & Tchekhovskoy (2017), allowing it to fall through the inner boundary unimpeded. Then, on a cell-by-cell basis, we measure the flux of kinetic, thermal, and radiative energy flowing through the boundary and return a fraction (albedo) of that energy as outflowing radiation. In the calculations reported in this Letter, that fraction corresponds to 75%, but a full study of this boundary condition for different values of the albedo is underway. An important consideration is the actual flux of radiation that crosses the inner boundary, which is controlled by the Riemann solver. The ghost cells are set to reflect 75% of the inflowing energy *in the ghost cells*. The HLL Riemann solver should pick a value that is roughly halfway between these two[6] fluxes and so in actuality we expect about 12.5% of the radiation flux to escape from the domain through the inner boundary.

We run the simulation for $80{,}000\,t_g$ where $t_g = GM\,c^{-3}$. Normally, in 2D axisymmetry, the absence of a dynamo driven by turbulence from the magnetorotational instability (MRI) leads to decay of the magnetic field. This is remedied with the use of a mean-field dynamo that restores the magnetic field in the accretion disk as a model for how it would be regenerated in 3D (Sądowski et al. 2015).

3. Simulation Results

The field lines of the stellar dipole are deformed to wrap around the initial torus, and so far from the star they are out of equilibrium. As the simulation starts, the magnetic field quickly relaxes to a stable configuration enveloping the torus while the closed loops near the star are virtually unchanged.

The torus begins to evolve as the MRI builds up and the gas begins to accrete. When the gas reaches the stellar magnetic field, it forces it inward, raising the magnetic pressure until it balances the ram pressure, at which point the gas begins to slide along magnetic field lines, forming accretion columns. As the gas hits the inner boundary, it is shocked and a large amount of radiation begins to leave the base of the column perpendicularly through the column's sides. As the simulation progresses, the accretion disk converges at progressively larger radii to its steady-state solution, launching outflows that collimate the radiation released in the columns and inner parts of the disk by confining it to a funnel-like region about the polar axis.

A snapshot from the simulation at time $t = 32{,}000\,t_g$ is shown in the upper panel of Figure 1. The lower panel depicts a time average from $t = 40{,}000\,t_g$ to $t = 80{,}000\,t_g$. The left half of the panel shows $\widehat{E}$, the radiation energy density in the fluid frame, and the right half of the panel shows the gas rest-mass density.

The magnetic field of the torus is oriented to be opposite in direction to the dipole field when they meet, leading to reconnection that allows gas to flow smoothly into the accretion columns (Parfrey & Tchekhovskoy 2017). The snapshot shows the remnant of a loop from the torus that had just reconnected with the stellar dipole in the disk midplane, indicated by the bold contour in the upper panel.

[6] The left-biased flux is determined by the ghost cells and the right-biased flux by the domain.

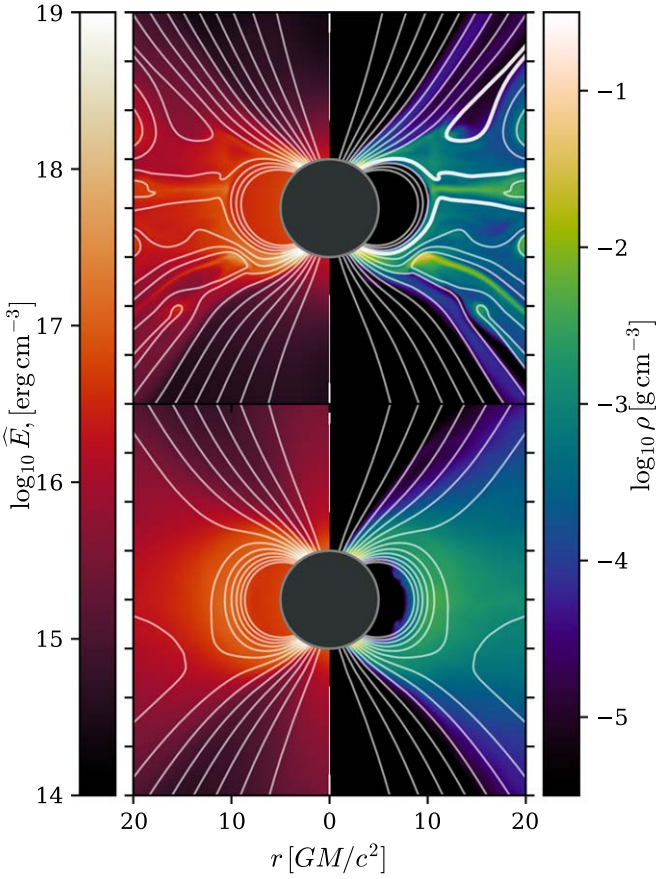

Figure 1. Snapshot (upper) and time-averaged (lower) plots of the radiation energy density (left), and the gas rest-mass density (right). We plot equispaced contours of A_ϕ, the ϕ component of the vector potential, which correspond to poloidal field lines due to the axisymmetric nature of the problem. A bold contour shows the remnant of a torus loop that had just reconnected with the neutron star's dipole.

The flow is quite turbulent. The snapshot captures a moment of lower luminosity before a high-density parcel of gas below the disk midplane enters the column and collides with the stellar surface, raising the luminosity significantly. The long-term effect of successive gas parcels hitting the surface and becoming shocked contributes to the steep radial gradient of radiation energy and gas density at the base of the column. This effect is also apparent from the difference in radiation energies in the polar region between the two panels. It is also evident that the polar region is largely devoid of gas. The gas is confined by the magnetic field to midlatitudes, strongly contrasting to what was observed in Abarca et al. (2018), where the absence of a stellar magnetic field allowed outflowing gas to fill the whole domain.

We can study the outflowing gas in more detail by considering the azimuthally integrated radial fluxes of gas and radiation, which are shown in Figure 2. The left half of the panel is the quantity $2\pi r\,\sin(\theta) F^r$ in units of $[L_{\rm Edd}\,r_g^{-1}]$, where $F^r = R^r{}_t$ is the radial component of the radiation flux (or momentum depending on the factor of c). One can then integrate by eye over $r\,\mathrm{d}\theta$ to estimate the luminosity. In a similar way, the gas momentum is integrated into the poloidal plane giving $2\pi r\,\sin(\theta)\rho u^r$ in units of $[L_{\rm Edd}\,r_g^{-1}c^{-2}]$.

Three contours are included. The solid green line shows the photosphere defined by $\tau_r = 1$, where τ_r is the scattering optical depth found by integrating from the outer boundary of the

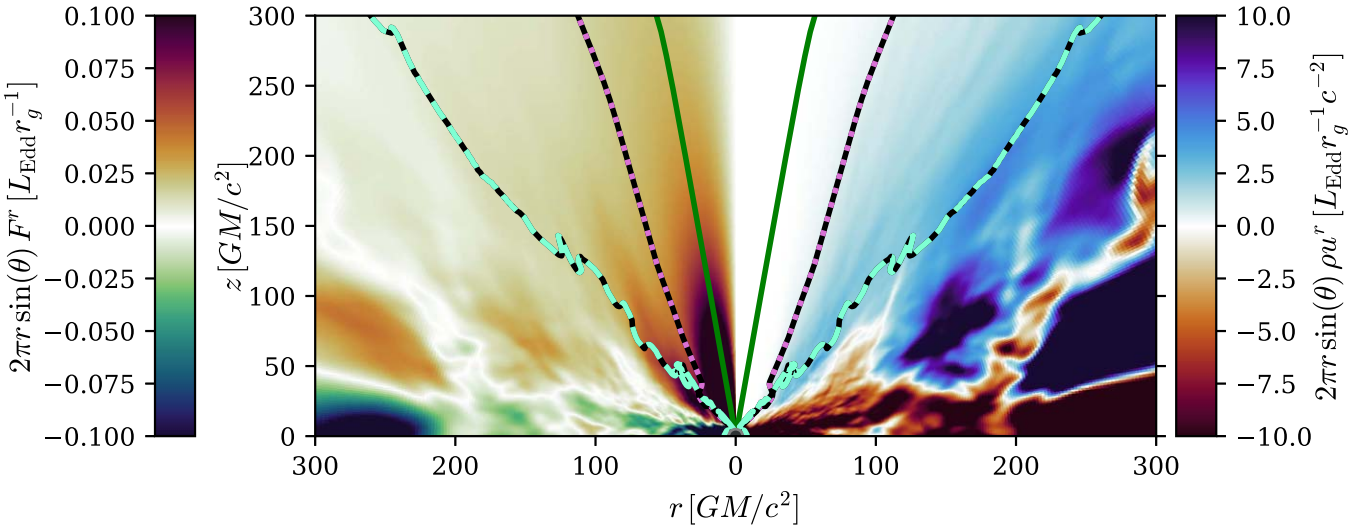

Figure 2. Radial radiative flux, $F^r = R_t^r$ (left), and gas momentum density, ρu^r (right), integrated into the poloidal plane. Overplotted in solid green is the photosphere at electron scattering depth unity, as measured radially, $\tau_r = 1$. The dashed pink and black line shows the photosphere as measured along the θ direction from the axis. The dashed teal and black line shows the zero-Bernoulli surface, Be = 0.

simulation to radius r. We can then assume that all of the outflowing radiation above this surface will reach the observer giving us a lower limit on the luminosity if we integrate the flux over the θ coordinate. By definition we can see very little gas above this surface, and all of the radiation that is between this line and the axis is expected to reach infinity. The polar region is completely dominated by a nearly radial flow of radiation escaping the inner region of the simulation. Surprisingly, a significant fraction of outgoing radiation is excluded by the $\tau_r = 1$ surface. There is very little momentum density in the corresponding region so one would expect the gas to be optically thin, and for this to be reflected in the $\tau_r = 1$ contour. However, the outflows do not flow exactly radially, nor in perfectly straight lines, so the gas at larger radii is obscuring the inner region. The flux at low radii, however, does not know about this gas and freely streams over a larger range of angles than indicated by the $\tau_r = 1$ surface. At some point (in our simulation between radius 300 and 400 r_g) the radiation scatters off the outflowing gas, becoming more confined. This is precisely the radiation-collimation effect that should lead to large apparent luminosities.

Another consideration is the small density gradient in the radial direction. This leads to the location of the photosphere being quite sensitive to small variations in the density and the precise value of the scattering cross section. The draconian approach of including 100% of the flux on one side of the contour and excluding 100% of the flux below the contour may not be appropriate for estimating the total luminosity, as the photons located immediately above and below the contour have almost the same probability of reaching the observer.

We can also measure the optical depth by integrating along θ from the axis. This surface, $\tau_\theta = 1$, is shown in Figure 2 by the densely dashed pink and black line. Because τ_θ is more useful for measuring the amount of radiation that leaves the accretion columns (since radiation escapes the column along the θ direction), it might provide a more accurate representation of the radiation that can reach the observer. The gradient of density along θ is much stronger than in the radial direction so there is much less uncertainty in the location of the photosphere in this direction. We can see that τ_θ is a good indicator for separating the very strong radiation flow near the axis from the less intense radiation flow in the gas outflows. Also, τ_θ is not affected by the geometry of the outflow at large radii; however, the question remains what happens to the radiation at large radii, or the radiation that scatters off of the side of the outflow near the accretion column?

The last curve, shown in loosely dashed teal and black represents the surface where the relativistic Bernoulli parameter,

$$Be = -\frac{T^t{}_t + R^t{}_t + \rho u^t}{\rho u^t}, \tag{7}$$

is equal to zero. This surface approximately splits the domain into energetically bound and unbound regions. Outflowing gas along this contour would be able to reach infinity with zero specific energy if it absorbed all of the radiative energy at its location. In reality, at some point the outflow should become diffuse enough that the radiation escapes. We can therefore use the zero-Bernoulli surface to define a region above which we can integrate the radiation flux to get an upper limit on the luminosity. If the gas rapidly becomes optically thin, the luminosity will be close to the integral of flux above this surface. It is more likely that the radiation deposits some of its momentum into the outflowing gas, lowering the luminosity. One could argue that it is also possible for the gas to cool contributing even more radiation to the total and exceeding this upper limit. However, we can verify that, at least in the simulation domain at radii larger than $\sim 70\, r_g$, the outflows almost exclusively absorb radiation.[7]

If we perform the integrals of radiative flux over spherical shells bounded by these three surfaces, we can plot the luminosity for each measure as a function of radius as shown in Figure 3. In addition to the three luminosities described above, for reference we also plot the total luminosity as integrated over the entire domain. Formally we can define the luminosities as

[7] Radiation transfers energy from the hot inner region to the cooler adiabatically expanding gas in the outer regions.

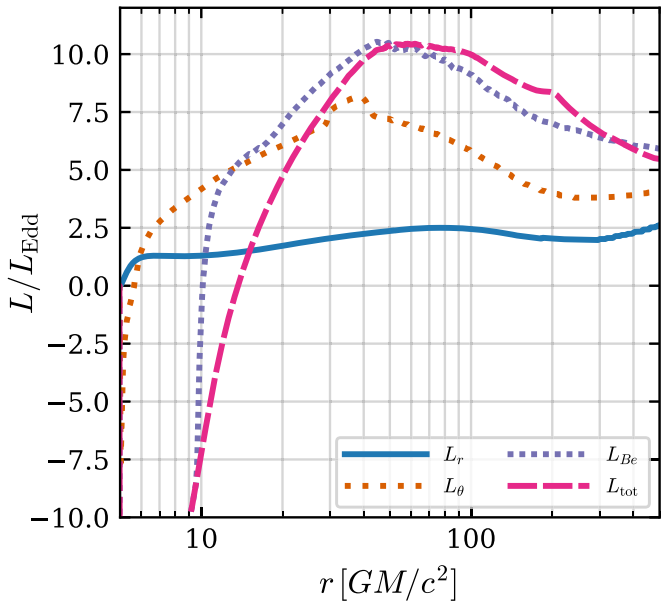

Figure 3. Four measures of the luminosity are plotted as a function of radius. In solid blue is L_r, loosely dotted orange shows L_θ, densely dotted purple is $L_{\rm Be}$, and dashed pink is $L_{\rm tot}$.

follows:

$$L_r = \int_{\tau_r<1} R^r{}_t \sqrt{-g}\ \mathrm{d}\theta, \tag{8}$$

$$L_\theta = \int_{\tau_\theta<1} R^r{}_t \sqrt{-g}\ \mathrm{d}\theta, \tag{9}$$

$$L_{\rm Be} = \int_{\rm Be>0} R^r{}_t \sqrt{-g}\ \mathrm{d}\theta, \tag{10}$$

$$L_{\rm tot} = \int_0^\pi R^r{}_t \sqrt{-g}\ \mathrm{d}\theta. \tag{11}$$

In steady state, the luminosity of a central radiation source would be constant (apart from redshift factors) with radius if radiative energy were conserved. However, the presence of gas, which can absorb and emit radiation, can change the shape of the luminosity curve even in steady state. Additionally, because optical depth is defined along coordinates, and not along the path of photons, it is possible to arbitrarily add or subtract to the luminosity curve if the average path of the photons is more complex, such as near the accretion columns.

We have run the simulation for a sufficiently long duration and taken a sufficiently long time average that the accretion disk should have reached a steady state out to radius 60–70 r_g and most of the turbulence should average away. The disk converges outward as the simulation runtime approaches the viscous time at a particular radius. The outflows, which have much larger velocity, converge much faster. A weak convergence condition for the outflow can be given by $r/v^r < t_{\rm avg}$, where $v^r = u^r/u^t$ is the coordinate velocity, and $t_{\rm avg}$ is the time period over which the simulation data were averaged. Our data are averaged over a long enough period of time that nearly the entirety of the gas outflow is able to satisfy the convergence condition. However, one must also take into account the origin of the outflow. A large portion of the outflowing gas originates from regions of the disk that have not yet converged, and as we explain later, this introduces uncertainty into some measures of the luminosity, especially at larger radii.

Despite all of this, L_r, shown as the solid blue line, is somewhat flat out to about radius $\sim 500\,r_g$ and so we believe that $L_r \approx 2.5\,L_{\rm Edd}$ is a good measure of the total radiative output of the simulation or at least a suitable lower limit. The steady rise up to radius $80\,r_g$ is probably due to radiation being emitted in and emerging from the outflows. Beyond, it is hard to determine whether the fluctuations are geometrical, or due to the unconverged nature of the simulation at large radii.

$L_{\rm Be}$, $L_{\rm tot}$, and L_θ, all show negative values near the star. This is related to the well-understood phenomenon of photon trapping in super-Eddington accretion disks (Ohsuga et al. 2002; Sądowski & Narayan 2016). Most of the radiation is advected inward by the optically thick gas before it can diffuse out of the disk. In our neutron-star case some of this energy is released at the surface. It would appear the photon-trapping effect is so strong that even with an albedo of 75%, inflowing radiation in the accretion columns dominates energy transport near the stellar surface. $L_{\rm tot}$ is also largely dominated by the advection of photons in the accretion columns and continues to decrease all the way to the surface.

Both L_r and L_θ rise steeply over the first r_g or so above the star due to the radiation shock. L_θ continues to rise as the accretion columns and accretion disk add to the luminosity. L_θ includes radiation released from the outflow below radius $\sim 70\,r_g$. At larger radii G_t switches sign, and the radiation contributing to L_θ passes through enough gas to deposit almost half of its momentum into the outflow lowering the luminosity to a local minimum of $\sim 3.75 L_{\rm Edd}$. The location of the $\tau_\theta = 1$ surface is unaffected by the outer boundary so the steady rise in L_θ above $r \sim 200\,r_g$ is likely due to the gas becoming steadily thinner, allowing more of the flux to contribute to the luminosity.

A similar effect is seen in $L_{\rm Be}$ and $L_{\rm tot}$. They rise sharply with increasing r up to $r \sim 60\,r_g$, as there is a significant amount of radiation advected with the outflow, and then drop as momentum starts to be transferred to the gas. $L_{\rm Be}$ is integrated over regions of the outflow that originate from parts of the disk that have not yet converged, especially beyond radius $r \sim 100\,r_g$, which increases the uncertainty in its value, especially at larger radii. $L_{\rm Be}$ largely follows $L_{\rm tot}$, although this appears to be largely a coincidence and is due to the equal amounts of radiation flowing inward and outward over the region where $Be < 0$.

4. Beamed Emission

The most important quantity, which is the signature of all ULXs, is a large apparent isotropic luminosity, that is, $L_{\rm iso} = 4\pi d^2 F$, measured from an observed flux, F, emitted by an object at a distance, d, away from the observer (neglecting cosmological effects). While it is impossible to predict $L_{\rm iso}$ reliably from the simulation data without sophisticated radiation post-processing, we can estimate it at a few locations in the simulation and see how it changes with radius. Plotted in the left panel of Figure 4 is $L_{\rm iso}$ as a function of viewing angle for different radii. The figure is presented in polar coordinates to emphasize the beaming pattern. One can immediately see that the vast majority of the flux is confined within 20° of the axis. The peak $L_{\rm iso}$ lies along the axis, and while it decays with radius (from the continuous green line through the dashed lines to the dotted one), it appears to be converging to a large value well above $100\,L_{\rm Edd}$ that is about $2 \times 10^{40}\,{\rm erg\,s^{-1}}$ for a canonical $1.4\,M_\odot$ neutron star.

The apparent luminosity is clearly bright enough for the neutron star to qualify as a ULX. To compare the measured

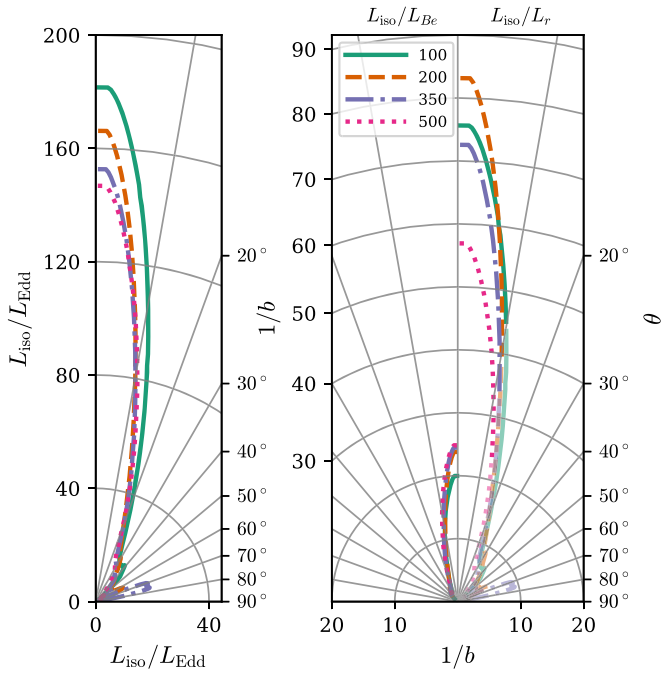

Figure 4. Inferred isotropic flux (left) and beaming pattern (right) as a function of viewing angle, measured from the pole. For the left panel, the radial coordinate corresponds to the isotropic luminosity, $L_{\rm iso} = 4\pi r^2 F^r$. For the right panel, the radial coordinate measures beaming, $1/b$, i.e., the inferred isotropic luminosity as a function of angle divided by the total luminosity. The left side of the right panel is a lower limit for $1/b$ obtained with the total luminosity, $L_{\rm Be}$. The right side of the right panel assumes the total luminosity is L_r, which provides an upper limit on $1/b$. All the quantities are measured at specific radii in the simulation, as indicated by the legend.

degree of beaming with the KLK model, we need to choose a quantity to function as the total luminosity. We consider L_r and $L_{\rm Be}$ as lower and upper limits, respectively (although we are confident that the true luminosity is much closer to L_r). These also correspond to lower and upper limits for the beaming factor $b = L/L_{\rm iso}$.

Near the axis, $L_{\rm iso}/L_{\rm Be} \sim 25$, and is more or less constant with radius. This already exceeds $1/b$ as computed from the KLK model (King et al. 2017; King & Lasota 2019, 2020) for all the sources they included. If we instead consider $L_{\rm iso}/L_r$, then $1/b$ shoots up to above 80. It falls at larger radii, to around 60.[8]

Note that the beaming factor is a function of the angle. In general, $1/b$ is proportional to flux, which is a function of θ, and lower viewing angles will tend to display more extreme beaming (corresponding to smaller values of b).

An important consideration is the effect that axisymmetry has on our simulation. Sądowski & Narayan (2016) compared a 2D axisymmetric accretion disk simulation onto a black hole to an identical simulation in 3D. The authors found that both of the simulations were remarkably similar, although the authors did notice that the degree of beaming was overestimated in the 2D simulation by a factor of about 2. We expect a similar degree of exaggerated beaming because the mechanism that collimates radiation is the same in both works. This could lower our estimated apparent isotropic flux to be around 10^{40} erg s^{-1}, which is still well in the realm of observed ULX luminosities.

Regardless of the measure used to compute the total luminosity, we have shown that a low-magnetic-field neutron star can produce emission that is sufficiently beamed to produce a ULX. The closest theoretical model to our simulation, the KLK model, also predicts large amounts of beaming, although not as extreme as we observe. The two models need not completely agree since they differ in several ways. The disk in our simulation has a very large spherization radius when compared to the magnetospheric radius. The KLK model requires that these two radii be much closer. This would substantially affect the outflows, as they are only launched below $r_{\rm sph}$ and above $r_{\rm M}$. Including the spherization radius in the domain is challenging, first, because it takes a long time for the simulation to converge to such large radii, and second, because beyond $r_{\rm sph}$, the disk should be similar to a thin disk, and thin disks are notoriously difficult to simulate.

One issue, although one that we already have plans to remedy, is the limitations of `Koral` when simulating the radiation field. `Koral` is a gray code that uses the M_1 closure scheme to transport radiation. M_1 works well for large extended sources, but when radiation originating from two or more distinct locations collide, the beams interact. For us, this is most problematic in the region directly outside of the accretion columns. The radiation flows toward the axis and is then directed upward due to the polar boundary condition, which is reflective. In reality, we expect the beams from the accretion columns to scatter off of the opposite wall formed by the gas outflows. After enough scatterings, the radiation should be collimated and largely moving along the axis. From Figure 1 we can see that the radiation already appears collimated as soon as it leaves the accretion column.

To get a more accurate representation of the radiation field, we need to go beyond the M_1 scheme. `HEROIC` (Narayan et al. 2016) is a postprocessing radiative transfer code that could be used to recompute the radiation field and spectrum for an observer at infinity as a function of viewing angle. While such calculations are out of the scope of this Letter, we plan to apply `HEROIC` postprocessing analysis to the rest of our simulations in a future publication.

5. Summary and Conclusions

We performed a 2D axisymmetric GRRMHD simulation of accretion onto a neutron star with a 2×10^{10} G dipolar magnetic field. The combination of the hard surface and confinement of the gas into accretion columns by the stellar magnetic field near the stellar surface allows the flow to release radiative energy at a rate of several times the Eddington limit. The fraction of this energy that is able to reach the observer, as opposed to being absorbed by the outflows, is difficult to calculate, but a lower limit of the observable luminosity should correspond to about $2.5\,L_{\rm Edd}$. The radiation easily escapes into the polar region, which is largely devoid of gas due to a combination of the magnetic field and rotation of the outflowing gas that collimates the radiation flow. While a more precise calculation of the radiation field is required due to the limitations of the simulation, our results show that this escaping radiation will be highly beamed. The apparent isotropic luminosity of the source observed pole-on should be on the order of $100\,L_{\rm Edd}$. This is encouraging if we wish to

[8] As r increases τ_r feels the effect of a finite outer boundary, so it is possible that the computed value of L_r may be slightly overestimated, leading to a slightly underestimated $1/b$ at large radii.

interpret the accreting system as a model of a neutron-star-powered ULX.

When compared to the KLK model (King et al. 2017; King & Lasota 2019, 2020), we find that the intensity of the beaming is larger, although we have reason to believe that postprocessing would show a less intensely beamed distribution of radiation at infinity. Furthermore, our simulation does not model the same system as considered by KLK. The distance between the Alfvén radius and spherization radius is large. We hope to produce simulations in future studies that can reproduce additional observable features of ULXs and that can provide more information about the nature of the magnetic field in pulsating and nonpulsating ULXs.

D.A. thanks Aleksander Sądowski and Andrew Chael for guidance on working with the `Koral` code; Maciek Wielgus, Miljenko Čemeljić, Jean-Pierre Lasota, and Alexander Tchekhovskoy for their advice, suggestions, and useful conversations; and Katarzyna Rusinek-Abarca for support, companionship, and patience. D.A. was supported in part by Polish National Science Center (NCN) Preludium grant 2017/27/N/ST9/00992. Research supported in part by NCN grant 2019/33/B/ST9/01564. Computations in this work were carried out on the Cyfronet Prometheus cluster, part of the PLGrid computing network.

Facility: Cyfronet Prometheus.

Software: Numpy (van der Walt et al. 2011; Harris et al. 2020), Scipy (Virtanen et al. 2020), matplotlib (Hunter 2007), pandas (McKinney 2010), Koral (Sądowski et al. 2013, 2015).

ORCID iDs

David Abarca https://orcid.org/0000-0002-9202-8734
Kyle Parfrey https://orcid.org/0000-0001-6173-0099
Włodek Kluźniak https://orcid.org/0000-0001-9043-8062

References

Abarca, D., Kluźniak, W., & Sądowski, A. 2018, MNRAS, 479, 3936
Abramowicz, M., Jaroszynski, M., & Sikora, M. 1978, A&A, 63, 221
Abramowicz, M. A., Czerny, B., Lasota, J. P., & Szuszkiewicz, E. 1988, ApJ, 332, 646
Bachetti, M., Harrison, F. A., Walton, D. J., et al. 2014, Natur, 514, 202
Begelman, M. C. 1978, MNRAS, 184, 53
Brightman, M., Harrison, F. A., Fürst, F., et al. 2018, NatAs, 2, 312
Carpano, S., Haberl, F., Maitra, C., & Vasilopoulos, G. 2018, MNRAS, 476, L45
Chandra, A. D., Roy, J., Agrawal, P. C., & Choudhury, M. 2020, MNRAS, 495, 2664
Czerny, B. 2019, Univ, 5, 131
Doroshenko, V., Tsygankov, S., & Santangelo, A. 2018, A&A, 613, A19
Fürst, F., Walton, D. J., Harrison, F. A., et al. 2016, ApJL, 831, L14
Fürst, F., Walton, D. J., Heida, M., et al. 2018, A&A, 616, A186
Harris, C. R., Millman, K. J., van der Walt, S. J., et al. 2020, Natur, 585, 357
Heida, M., Lau, R. M., Davies, B., et al. 2019, ApJL, 883, L34
Hunter, J. D. 2007, CSE, 9, 90
Israel, G. L., Belfiore, A., Stella, L., et al. 2017a, Sci, 355, 817
Israel, G. L., Papitto, A., Esposito, P., et al. 2017b, MNRAS, 466, L48
Kaaret, P., Feng, H., & Roberts, T. P. 2017, ARA&A, 55, 303
King, A., & Lasota, J.-P. 2019, MNRAS, 485, 3588
King, A., & Lasota, J.-P. 2020, MNRAS, 494, 3611
King, A., Lasota, J.-P., & Kluźniak, W. 2017, MNRAS, 468, L59
King, A. R., Davies, M. B., Ward, M. J., Fabbiano, G., & Elvis, M. 2001, ApJL, 552, L109
Kluźniak, W., & Lasota, J.-P. 2015, MNRAS, 448, L43
Kluzniak, W., & Wagoner, R. V. 1985, ApJ, 297, 548
McKinney, W. 2010, Proc. SciPy, 9, 56
Mihalas, D., & Mihalas, B. W. 1984, Foundations of Radiation Hydrodynamics (New York: Oxford Univ. Press)
Motch, C., Pakull, M. W., Soria, R., Grisé, F., & Pietrzyński, G. 2014, Natur, 514, 198
Mushtukov, A. A., Portegies Zwart, S., Tsygankov, S. S., Nagirner, D. I., & Poutanen, J. 2021, MNRAS, 501, 2424
Mushtukov, A. A., Suleimanov, V. F., Tsygankov, S. S., & Ingram, A. 2017, MNRAS, 467, 1202
Narayan, R., Zhu, Y., Psaltis, D., & Sądowski, A. 2016, MNRAS, 457, 608
Ohsuga, K., Mineshige, S., Mori, M., & Umemura, M. 2002, ApJ, 574, 315
Paczyński, B., & Wiita, P. J. 1980, A&A, 500, 203
Parfrey, K., & Tchekhovskoy, A. 2017, ApJL, 851, L34
Penna, R. F., Kulkarni, A., & Narayan, R. 2013, A&A, 559, A116
Riley, T. E., Watts, A. L., Bogdanov, S., et al. 2019, ApJL, 887, L21
Sądowski, A., & Narayan, R. 2016, MNRAS, 456, 3929
Sądowski, A., Narayan, R., Tchekhovskoy, A., et al. 2015, MNRAS, 447, 49
Sądowski, A., Narayan, R., Tchekhovskoy, A., & Zhu, Y. 2013, MNRAS, 429, 3533
Shakura, N. I., & Sunyaev, R. A. 1973, A&A, 24, 337
Syunyaev, R. A., & Shakura, N. I. 1986, SvAL, 12, 117
Takahashi, H. R., Mineshige, S., & Ohsuga, K. 2018, ApJ, 853, 45
Takahashi, H. R., & Ohsuga, K. 2017, ApJL, 845, L9
Tóth, G. 2000, JCoPh, 161, 605
Townsend, L. J., Kennea, J. A., Coe, M. J., et al. 2017, MNRAS, 471, 3878
Trudolyubov, S. P. 2008, MNRAS, 387, L36
Tsygankov, S. S., Doroshenko, V., Lutovinov, A. A., Mushtukov, A. A., & Poutanen, J. 2017, A&A, 605, A39
van der Walt, S., Colbert, S. C., & Varoquaux, G. 2011, CSE, 13, 22
Virtanen, P., Gommers, R., Oliphant, T. E., et al. 2020, NatMe, 17, 261
Wasserman, I., & Shapiro, S. L. 1983, ApJ, 265, 1036